PAPER • OPEN ACCESS

Cryogenic trapped-ion system for large scale quantum simulation

View the article online for updates and enhancements.

IOP ebooks™

Bringing you innovative digital publishing with leading voices to create your essential collection of books in STEM research.

Start exploring the collection - download the first chapter of every title for free.

Quantum Science and Technology

PAPER

Cryogenic trapped-ion system for large scale quantum simulation

G Pagano[1,6] , P W Hess[2] , H B Kaplan[1], W L Tan[1], P Richerme[3], P Becker[1], A Kyprianidis[1], J Zhang[1],
E Birckelbaw[1], M R Hernandez[1], Y Wu[4] and C Monroe[1,5]

[1] Joint Quantum Institute, Department of Physics and Joint Center for Quantum Information and Computer Science, University of Maryland, College Park, MD 20742, United States of America
[2] Middlebury College Department of Physics, Middlebury, VT 05753, United States of America
[3] Department of Physics, Indiana University, Bloomington, IN 47405, United States of America
[4] Department of Physics, University of Michigan, Ann Arbor, MI 48109, United States of America
[5] IonQ Inc., College Park, MD 20740, United States of America
[6] Author to whom any correspondence should be addressed.

E-mail: pagano@umd.edu

Keywords: ion trapping and cooling, cryogenics, atomic and molecular collisions, vacuum technology, quantum simulation

Abstract

Trapped-ion systems are among the most promising hardware candidates for large scale quantum computing and quantum simulation. In order to scale up such devices, it is necessary to engineer extreme-high vacuum (XHV) environments to prevent background gas from disrupting the ion crystal. Here we present a new cryogenic ion trapping system designed for long time storage of large ion chains. Our apparatus is based on a segmented-blade ion trap enclosed in a 4 K cryostat, which enables us to routinely trap and hold over 100 $^{171}Yb^+$ ions for hours in a linear configuration, due to low background gas pressure from differential cryo-pumping. We characterize the XHV cryogenic environment measuring pressures below 10^{-11} Torr by recording both inelastic and elastic collisions between the ion chain and the molecular background gas. We also demonstrate coherent one and two-qubit operations and nearly equidistant ion spacing for chains of up to 44 ions using anharmonic axial potentials, in order to enable better detection and single ion addressing in large ion arrays. We anticipate that this reliable production and lifetime enhancement of large linear ion chains will enable quantum simulation of models that are intractable with classical computer modeling.

1. Introduction

Atomic ions confined in radio-frequency (rf) Paul traps are one of the leading platforms for both quantum computing [1] and quantum simulation of interacting spin models [2–6], high energy physics [7, 8], quantum chemistry [9] and bosonic models [10]. As these systems become larger, classical simulation methods become incapable of modeling the exponentially growing Hilbert space, necessitating quantum simulation for precise predictions. Currently room temperature experiments at typical ultra-high-vacuum (UHV) pressures (10^{-11} Torr) are limited to about 50 ions due to collisions with background gas that regularly destroy the ion crystal [11]. The background pressure achievable in UHV vacuum chambers is ultimately limited by degassing of inner surfaces of the apparatus. However, cooling down the system to cryogenic temperatures turns the inner surfaces into getters that trap most of the residual background gases. This technique, called cryo-pumping, has led to the lowest level of vacuum ever observed ($< 5 \times 10^{-17}$ Torr) [12].

Here we report an experimental setup consisting of a macroscopic segmented blade trap into a cryogenic vacuum apparatus that allows for the trapping and storage of large chains of $^{171}Yb^+$ ions, one of the most promising qubit candidate for ion-trap based quantum simulation and computation. In section 2 we describe the apparatus, describing how the cryostat has been designed to allow high optical access within the cooling power limits of the cryocooler and to damp mechanical vibrations through an exchange gas region. We describe in detail the performance of the helical resonator supplying the radio-frequency (rf) drive to the ion trap, and the atomic source, placed in the room temperature region to avoid damage due to thermal gradients. In section 3 we report on the performance of the vibration isolation system (VIS). Through improvements to the mechanical stability of the whole structure inside the 4

K region, we managed to suppress vibrations of the apparatus that would otherwise add phase noise on the qubit, affecting the performance of the quantum simulator. In section 4 we show coherent operations on both one and two ^{171}Yb$^+$ qubits, proving that residual mechanical vibrations do not limit the capabilities of our apparatus for quantum simulation. In section 5 we show pressure measurements using the ion crystals themselves as a pressure gauge below 10^{-11} Torr. We characterize the dependence of the pressure on the cryostat temperature by measuring the inelastic and elastic collision rates of trapped ions with background H$_2$ molecules. In section 6 we show the capability to shape the axial potential in order to minimize the ion spacing inhomogeneity in large ion chains, and in section 7 we summarize perspectives for future experiments.
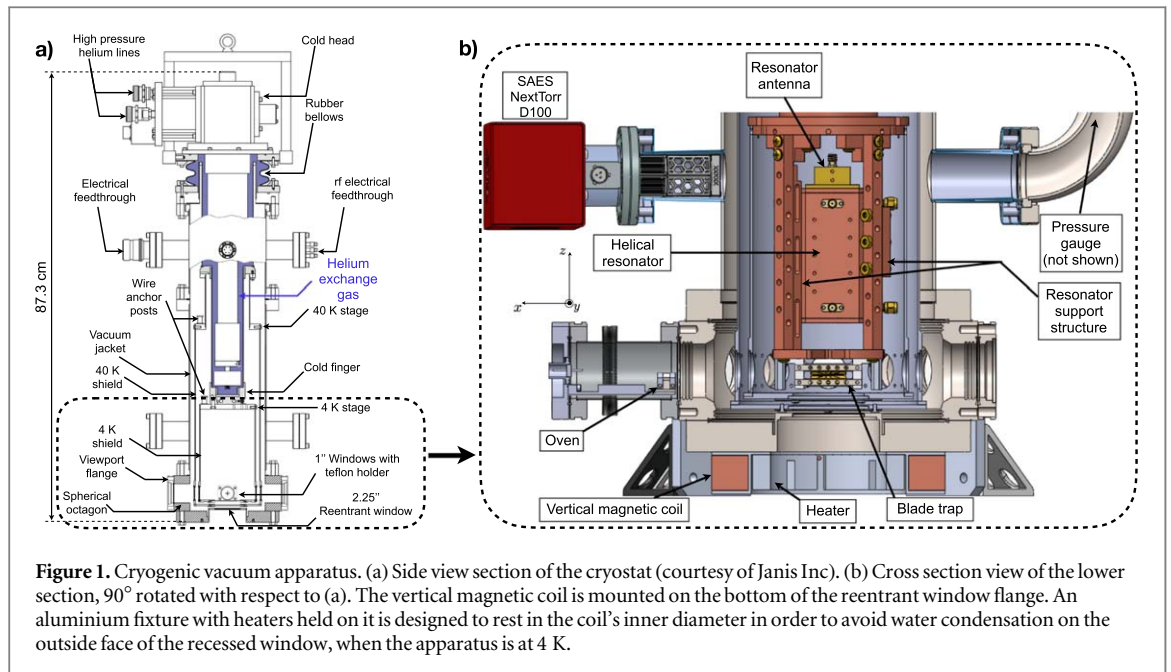
2. The apparatus

The challenge of merging atomic physics and ion trap technology with cryogenic engineering has been successfully undertaken by many groups around the world [13–19]. Cryogenic ion traps offer two remarkable advantages: Firstly, heating rates [20, 21] due to surface patch potential and electric field noise can be suppressed by orders of magnitude compared with room temperature traps, as it was first demonstrated in [14]. Secondly, the low pressures achievable via cryo-pumping reduce the collision rate with the residual background gas, thereby enhance the lifetime of the ions in the trap. Indeed, in standard UHV systems, the storage time of a large number of ions in a linear chain is typically limited by the probability that a 'catastrophic' collision event causes the ion crystal to melt and the ions to be ejected from the trap. Assuming that the collisional loss probability scales linearly with the number of ions, it is necessary to achieve a significant reduction in the background pressure in order to increase the capabilities of the trapped-ion quantum simulator platform. Recent pioneering techniques such as titanium coating and heat treatment [22] have been shown to achieve extreme-high vacuum (XHV) in room temperature vacuum systems. However, combining room temperature XHV with an ion trap apparatus remains a challenge because many components in the vacuum system may not be XHV-compatible, such as the common electrical insulators (Kapton or PEEK). On the other hand, with a cryogenic setup, beside a lower residual gas density with respect to UHV systems, there is the additional advantage of having a lower temperature residual background gas. For this reason, the ion–molecule collisions, even when they occur, are not harmful for the ion chain. Moreover, a cryogenic ion-trap apparatus can offer a significant background pressure reduction at 4 K while maintaining high optical access for ion addressing and detection. Therefore, careful design is required in order to: (a) minimize room temperature blackbody radiation without limiting optical access and (b) mechanically decouple the system from the cold head vibrations while maintaining significant cooling power at 4 K. The design and the performance of the cryogenic apparatus will be described in the next subsections.

2.1. The cryostat
In order to minimize the vibrations induced by the cryocooler, one possible choice is a flow cryostat [18] or a bath cryostat, which feature very low acoustic noise. However, these types of cryostats require continuous replenishment of cold liquid coolant, which is expensive and time-consuming. The alternative is to use a closed-cycle cryocooler which does not require liquid coolant to be constantly refilled and it is more convenient as it only needs external electric supply. However, a closed cycle cryocooler suffers from severe acoustic noise. To address this challenge, we decided to use a closed cycle Gifford–McMahon cryostat, whose vibrating cold finger is mechanically decoupled from the main vacuum apparatus through an exchange gas region (see figure 1(a)) filled with helium gas at a pressure of 1 psi above atmosphere. The helium gas serves as a thermal link between the cold finger and the sample mount to which the ion trap apparatus is attached. A rubber bellows is the only direct mechanical coupling between the vibrating cold head and the rest of the vacuum apparatus which is sitting on the optical breadboard. This VIS allows us to keep the vibrations rms amplitude below 70 nm (see section 3 for more details). During normal operation, the vibrating cold head is attached to the overhead equipment racks hanging from the ceiling and the vacuum apparatus is resting on an optical breadboard. However, by connecting the cold head and the cryostat mechanically, the entire system can be hoisted and moved from the optical breadboard to a freestanding structure where upgrades and repairs can be performed.

On top of the Cryostat (SHV-4XG-15-UHV), made by Janis Inc., sits a cold head (SRDK-415D2) that is powered by a F-70L Sumitomo helium compressor. The cold head features two stages with different cooling powers, 45 W for the 40 K stage and 1.5 W for the 4 K stage. In order to shield the ion trap apparatus from room temperature blackbody radiation (BBR), two aluminium concentric cylindrical radiation shields are in thermal contact with the two stages. Their BBR heat loads, estimated using the Stefan–Boltzmann law[7], are $\dot{Q}_{40K} \sim 5.5$ W and $\dot{Q}_{4K} \sim 550$ μW, well below the cooling power of the two heat stages.

---

[7] The radiation heat load $\dot{Q}$ on a given surface S at temperature T_0 from an environment at T_1 is given by the Stefan–Boltzmann law and it is proportional to $\dot{Q} = \sigma(T_1^4 - T_0^4)/V$ where $\sigma = 5.67 \times 10^{-8}$ W K^{-4} m^{-2} and V is the so called view, which is a function of the geometry, the surface S and their emissivities.

Figure 1. Cryogenic vacuum apparatus. (a) Side view section of the cryostat (courtesy of Janis Inc). (b) Cross section view of the lower section, 90° rotated with respect to (a). The vertical magnetic coil is mounted on the bottom of the reentrant window flange. An aluminium fixture with heaters held on it is designed to rest in the coil's inner diameter in order to avoid water condensation on the outside face of the recessed window, when the apparatus is at 4 K.
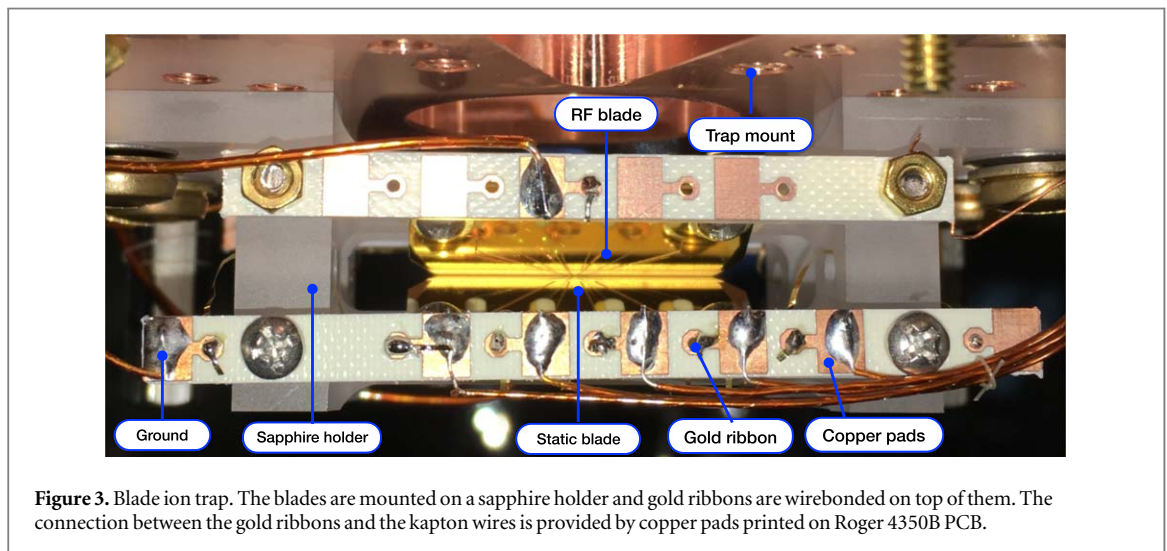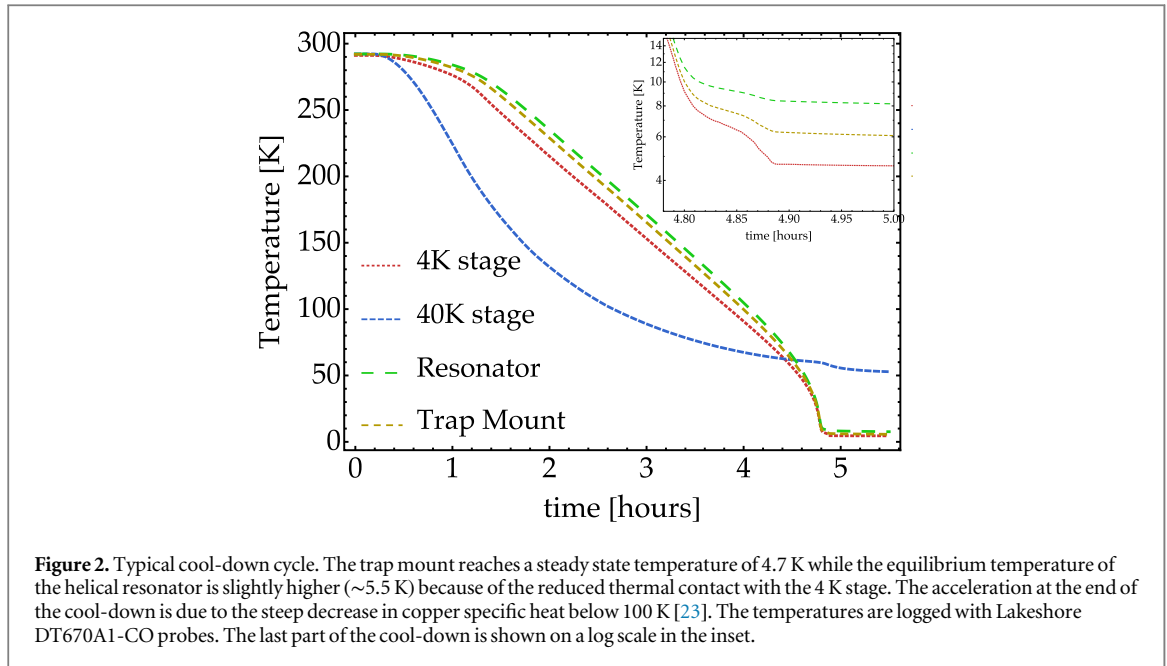
The thermal heat load on the trap due to the electrical wiring is estimated to be negligible (∼100 μW) since the temperature probes (Lakeshore DT670A1-CO), the static electrodes, and the ovens wires are all heat sunk to anchor posts (see figure 1(a)) in good thermal contact with both stages. The four SMA cables connected to the radio-frequency (rf) electrical feedthrough are not heat sunk and deliver an estimated heat load of 500 mW and 220 mW on the 40 K and 4 K stages, respectively[8]. In designing the apparatus, a good balance between room temperature BBR heat load and optical access has been achieved, given the total cooling power. The spherical octagon (see figure 1) features eight 1″ diameter windows which provide optical access in the x–y plane, held by soft teflon holders. On the bottom, the system features a 2.25″ diameter reentrant window which allows for a numerical aperture (NA) up to 0.5 to image the ions along the vertical (z) direction. The whole cryostat rests on an elevated breadboard to allow for ion imaging from underneath. The total heat load of the recessed window is estimated to be 2.4 W on the 40 K shield and 1.7 mW on the 4 K shield. The total heat load budget (see appendix A for details) is well below the total cooling power, and therefore we can cool the system down to 4.5 K in about 5 h (see temperature measurements in figure 2) with both the helical resonator and the ion trap inside the 4 K shield.

Before the cool down, the apparatus is pre-evacuated using a turbo-molecular pump until the pressure reading on the MKS-390511-0-YG-T gauge (not shown in figure 1(b)) reaches the pressure of about $\simeq 2 \times 10^{-5}$ Torr. The gauge is attached through an elbow in order to avoid direct 'line of sight' exposure of its radiative heat load (1.5 W) to the 40 K shield. Since hydrogen is the least efficiently cryo-pumped gas, we added a SAES NextTorr D-100 getter and ion pump (see figure 1(b)) which is attached to one of four CF40 flanges of the long bellow cross.

2.2. Blade trap

We chose to assemble a blade-style ion trap as it provides high optical access along all directions [24]. The trap was hand-assembled and aligned under a microscope with $\simeq 5$ μm resolution. The blades are made of alumina and have five segments. They were cleaned with hydrofluoric acid and plasma ashed on both sides, then coated with a 100 nm titanium adhesion layer and a 1 μm gold layer at Sandia Laboratories. The coating was applied by means of multi-directional evaporation to avoid alumina exposure in the 50 μm wide gaps between the segments. The two static electrode blades are gold coated with masks so that the five segments can be biased independently, whereas the rf blades have an unsegmented coating. Gold ribbons (0.015″ wide and 0.001″ thick) are wire-bonded on top of the blades for electrical connections. In order to shunt rf pickup voltages on the static blades, 800 pF ceramic capacitors connect each static electrode segment to ground. The capacitors (DIGIKEY 399-11198-1-ND) are made of NP0, whose capacitance has small temperature dependence down to 4 K. We chose to solder the capacitors onto the gold ribbons as we could not find any capacitor made of low dielectric constant material that could be wirebonded directly to the gold ribbon. Standard solder is cryo-compatible [23],

---

[8] The heat conduction contribution of the wiring has been estimated as $\dot{Q} = A \big/ L \int_{T_1}^{T_2} \lambda(T)\,\mathrm{d}T$, where A is the wire cross-section, L is the wire length and $\lambda(T)$ is the temperature dependent heat conductivity and T_1 and T_2 are the temperatures of the two ends of the wire [23].

Figure 2. Typical cool-down cycle. The trap mount reaches a steady state temperature of 4.7 K while the equilibrium temperature of the helical resonator is slightly higher (∼5.5 K) because of the reduced thermal contact with the 4 K stage. The acceleration at the end of the cool-down is due to the steep decrease in copper specific heat below 100 K [23]. The temperatures are logged with Lakeshore DT670A1-CO probes. The last part of the cool-down is shown on a log scale in the inset.

Figure 3. Blade ion trap. The blades are mounted on a sapphire holder and gold ribbons are wirebonded on top of them. The connection between the gold ribbons and the kapton wires is provided by copper pads printed on Roger 4350B PCB.

so we used it to connect the other end of the gold ribbons to the external copper pads (see figure 3) for wiring, instead of using the invasive spot-welding procedure usually followed for UHV blade traps. The blades are mounted on a sapphire holder in a 60°/30° angle configuration, which allows good optical access both in the *x*–*y* plane and along the vertical *z* direction, and strongly breaks rotational symmetry so that the trap principal axes are well-defined. The distances between the electrodes tips are 340 μm/140 μm and the ion-electrode distance is 180 μm. The *x*–*y* plane features 0.1 NA through the eight 1″ windows, which are used for Doppler cooling, detection, optical pumping (369 nm), photo-ionization (399 nm), repumping (935 nm) and Raman (355 nm) laser beams [25]. We can perform high-resolution imaging along the vertical *z* direction (see figure 1(b)) since we have a 3.5 cm working distance on a 2″ window, allowing for an objective of up to 0.5 NA. Figure 4 shows an image of a linear crystal of 121 laser-cooled ^{171}Yb$^+$ ions confined in the trap.

In order to provide eV-deep trapping potentials and high trap frequencies, the blade trap needs to be driven with hundreds of Volts in the radio-frequency range. Based on the COMSOL simulation model of the blade trap, we need about $V_{rf} = 480$ V amplitude to get a $\omega_{tr} = 2\pi \times 4$ MHz transverse trap frequency with a rf drive at $\Omega_{rf} = 2\pi \times 24$ MHz. Considering the calculated trap capacitance $C_t = 1.5$ pF, we can estimate the power dissipated [26] on the blades to be $P_d = \frac{1}{2}\Omega_{rf}^2 C_t^2 V_{rf}^2 R_t \simeq 1$ mW, where R_t is the resistance of the 1 μm gold layer on the blade, which is estimated considering that the gold skin depth is $\delta \simeq 250$ nm at 4 K. Moreover, the blades are efficiently heat sunk, as they are mounted on a holder made of sapphire, which presents the double advantage of a better thermal conductivity compared to macor or alumina holders and a well matched coefficient of thermal expansion with the alumina blade substrate.
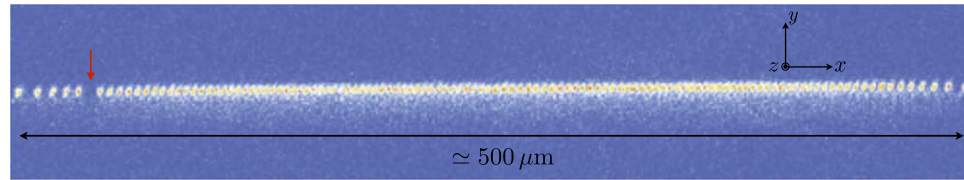
Figure 4. Linear chain of 121 ^{171}Yb$^+$ ions. In this case $\omega_y/2\pi = 1.5$ MHz and $\omega_x/2\pi = 35$ kHz. The axial confinement has been relaxed to resolve all the center ions with a 0.13 NA objective. In order to fit the whole chain in the CCD camera, we took two images of the left and right part of the chain by moving the objective along the trap axis. On the left side of the chain, a lone ^{171}Yb$^+$ ion in the $^2F_{7/2}$ state does not fluoresce, marked by the red arrow. This dark ion retained its position after more than 4 h indicating that the chain never melted due to collisions with the background gas.

2.3. Helical resonator

A helical resonator [27] enables impedance matching between a radiofrequency source and the trap by acting as a step-up transformer. The parasitic capacitance and inductance of the 70 cm coaxial rf transmission cable between the vacuum feedthrough and ion trap would make the impedance matching of the tuned resonator and trap circuit [28] very difficult, thereby limiting the rf voltage that could be delivered to the trap without incurring in resistive heating of the rf cables. Therefore, the apparatus is designed to host the helical resonator in the 4 K region as close as possible to the blade trap.

Inside the helical resonator, we have wound a bifilar coil whose two components are connected to the two rf blades. In this way, each blade can have an independent static potential offset. The two coils are held in place by teflon holders and they are shorted at rf with a 400 nF capacitor. The resonator is made of solid copper with a 2.3″ inner radius, whereas the bifilar coil features a 1.5″ radius and a 0.19″ pitch. We inserted a capacitive 100:1 pick-off of the rf voltage inside the resonator to monitor and actively stabilize the transmitted voltage amplitude to the trap blades [29]. The self-inductance $L_{res} = 2$ μH and self-capacitance $C_{res} = 8$ pF have been measured loading the resonator with different test-capacitors.

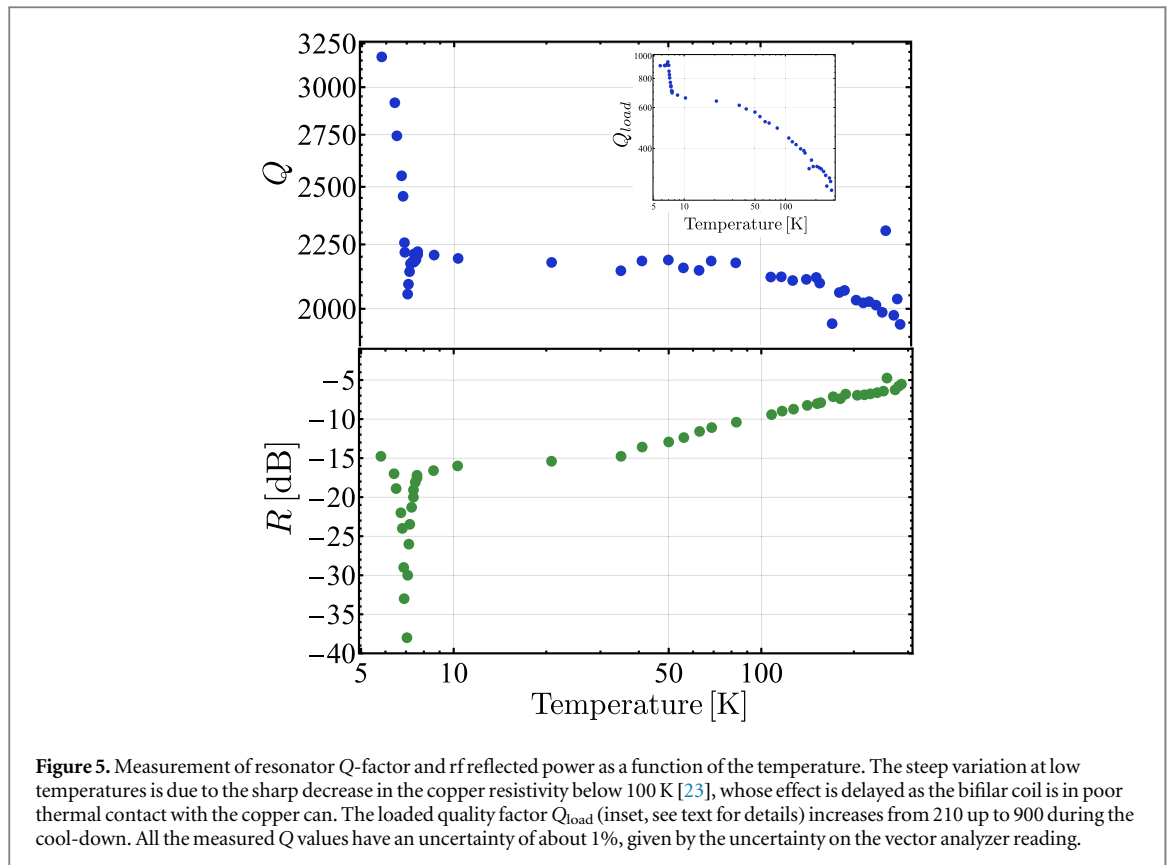At room temperature the intrinsic ('unloaded') resonator quality factor is $Q = 1050$, where Q is defined as:

$$Q = \frac{2\,Q_{load}}{1 - \sqrt{R}}, \qquad (1)$$

where R is the reflected rf power due to impedance mismatch (see figure 5) and $Q_{load} = \Omega_{rf}/\text{FWHM}$ is the loaded Q-factor, which takes into account also the impedance matching with the rf source. The resonator is inductively coupled with a small 0.5″ diameter antenna-coil, whose position can be tuned to reach critical coupling. At 4 K, the resistance of the whole rf circuit is reduced and two effects take place: the Q value at critical coupling increases up to 3170 and the impedance matching condition changes (see figure 5). The 60% increase in the resonator quality factor is lower than what would be expected from a simple estimate based on the decrease of copper resistivity and skin depth at 4 K. This is likely explained by oxide layers on the copper surface or by the additional resistance contribution of solder connections in the resonator. In order to compensate the temperature induced resistance change, we reduced the mutual inductance between the antenna and the bifilar coil by pulling out the antenna holder (see figure 1(b)) away from the optimal position at room temperature. During the cool-down, the drive frequency $\Omega_{rf}/2\pi$ increases typically by 0.6%, which is explained by the reduction in resonator self-capacitance and self-inductance induced by thermal contraction of the copper.

2.4. Atomic source

In order to load the ions in the blade trap we resistively heat up the atomic source, which is encased in a 0.5″ long stainless steel (SS) tube with a tantalum wire spot welded to each end. The oven is supported by a macor holder, made of two 0.05″ ID halves enclosing the SS tube to ensure stable pointing and to provide thermal insulation. We noted that having the atomic sources in the 4 K region, as close as possible to the trap to maximize the atomic flux, causes numerous problems: the heat load coming from the ovens was enough to make the whole copper structure expand more than the trap clearance, requiring the Doppler cooling beam to be steered accordingly for trapping. Moreover, the whole ramp up of the ovens had to be done gradually as the thermal gradients could break the tantalum wires, resulting in a total average loading time of 1 h and 30 min. For all these reasons, we decided to move the atomic source to the room temperature sector of the vacuum apparatus (see figure 1(b)).

The oven is in a 2.93″ long UHV bellow so that under vacuum the atomic source is 11.9 cm away from the trap. The atomic beam is collimated by two pinholes mounted on the 4 and 40 K shields and is aligned on the trap axis (x) to minimize the exposure of the electrode gaps. This prevents shorts or the formation of ytterbium oxide layers on the blades when the system is vented. The oven's macor holder sits on an aluminium bar which is screwed down to the feedthrough of the bellows and whose height is designed to match the trap axis location when the apparatus is cold (see figure 1(b)). The use of the bellows was originally intended to enable one to steer the atomic beam to maximize

Figure 5. Measurement of resonator Q-factor and rf reflected power as a function of the temperature. The steep variation at low temperatures is due to the sharp decrease in the copper resistivity below 100 K [23], whose effect is delayed as the bifilar coil is in poor thermal contact with the copper can. The loaded quality factor Q_{load} (inset, see text for details) increases from 210 up to 900 during the cool-down. All the measured Q values have an uncertainty of about 1%, given by the uncertainty on the vector analyzer reading.
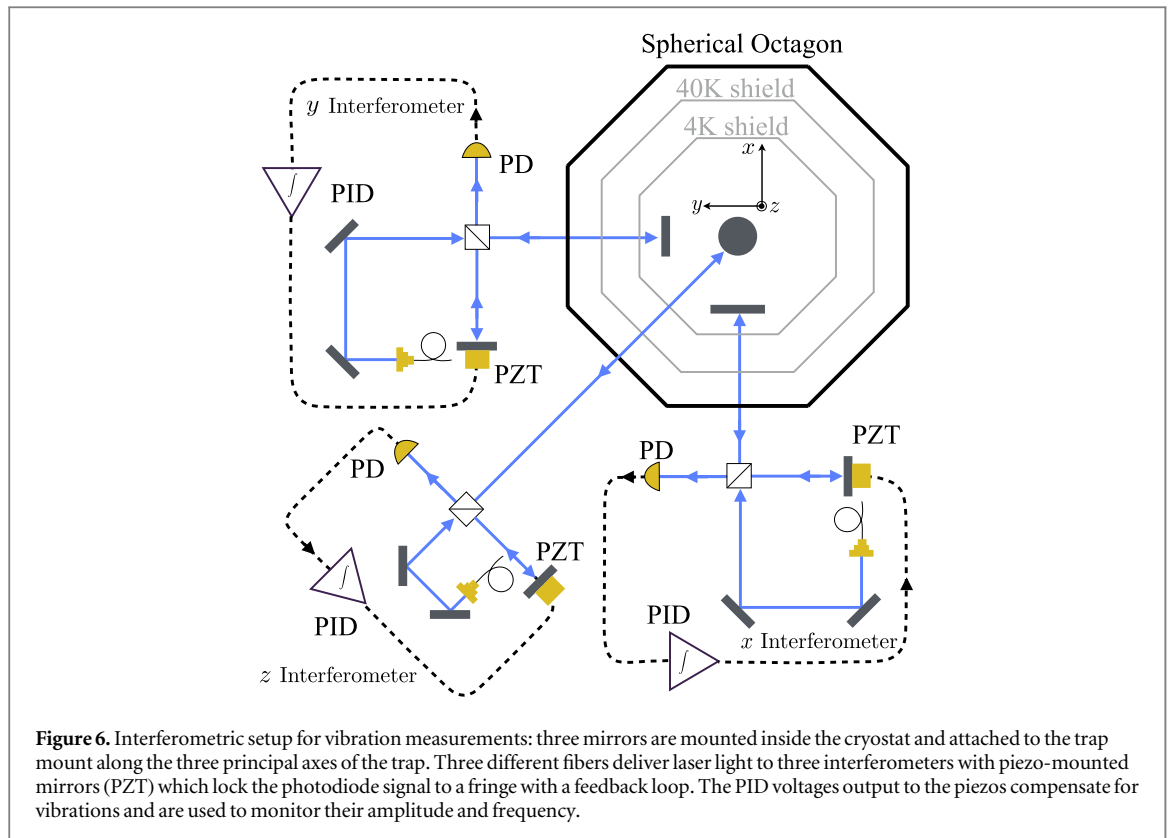
the loading rate, but the alignment by design was enough to provide a satisfactory loading rate. The generation of the atomic flux is achieved by the Joule effect, dissipating 1.5 W on the 0.22 Ohm oven resistance. With this setting, we can load about 50 ions in approximately 4 min (including oven warm-up time), a timescale comparable to other setups, using similar parameters (2 mW of 399 nm and 350 mW of 355 nm laser light) to perform a two-step photoionization process. It shall be noted that, even though the ion loading is a stochastic process, there is a strong correlation between the 355 nm photoionization laser being on and the number of ions increasing by one or two units. This makes loading the desired number of ions within one or two attempts possible.

3. Vibration isolation system

Since the Gifford–McMahon cold head compression and expansion cycles produce a significant amount of acoustic vibrations, it is crucial to assess and improve the performance of the VIS. This system consists of an exchange gas region filled with helium gas, to provide a thermal link between the vibrating cold head and the cold finger. A rubber bellows (see figure 1(a)) is the only mechanical connection between the cold head and the lower part of the apparatus and acts as a vibration damper.

We are interested in both the timescale and the amplitude of the residual acoustic vibrations. Indeed we plan to perform quantum simulation experiments lasting up to 10 ms, creating spin–spin interactions [3] through stimulated two-photon Raman processes driven by a pulsed laser at $\lambda = 355$ nm (see section 4). Therefore, any ion chain displacement of the order of λ during the laser interaction time would result in an unwanted phase shift experienced by the ions. We characterized the mechanical stability of the whole apparatus by interferometric measurements. We removed the trap and placed three mirrors on the trap mount, along the three principal axes: the Raman direction y, the trap axis x and the vertical imaging direction z (see figure 6). In this way, every movement of the trap region with respect to the breadboard and the table can be measured with a few nanometers resolution. In order to reliably assess the displacement of the trap by counting the number of fringes induced by the acoustic vibration, three piezo-mounted mirrors are used on the reference path of the Michelson interferometers to lock the interferometer to a fringe (see figure 6). The servo loops have 1.8 kHz bandwidth and therefore they can fully compensate acoustic noise over the frequency range of interest (up to 300 Hz). The voltage-to-distance conversion of the piezo-mounted mirrors has been characterized on a static interferometer: in this way, the output voltages applied to the piezos are a direct measurement of the displacement of the trap mount along the three principal axes of the trap.
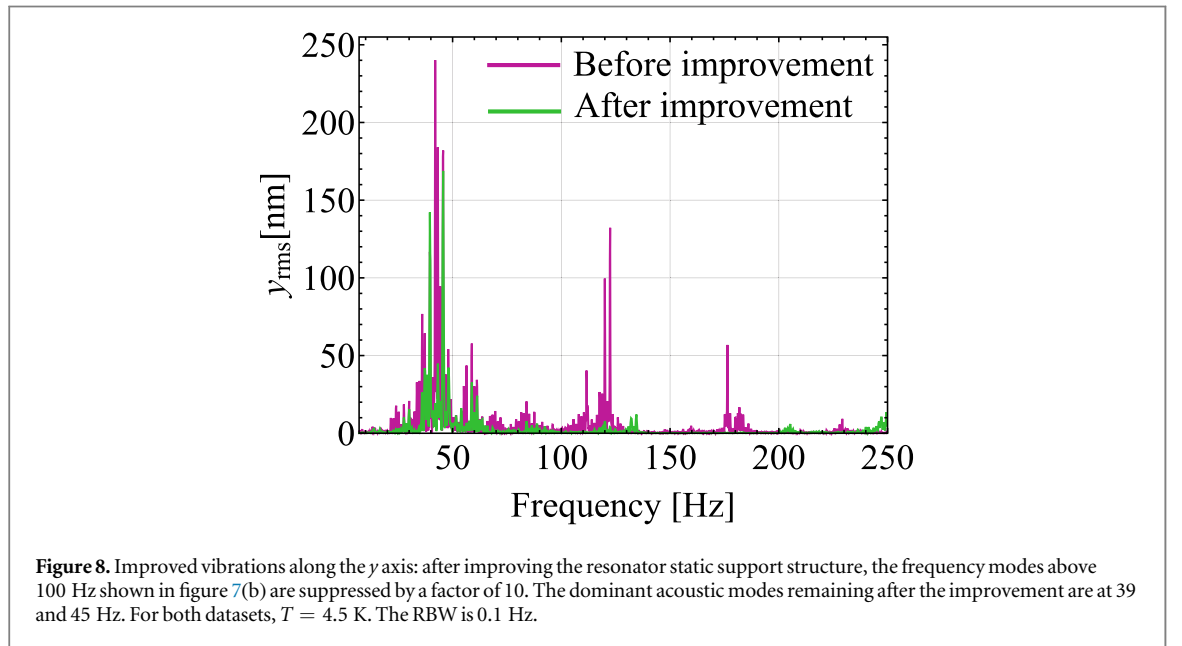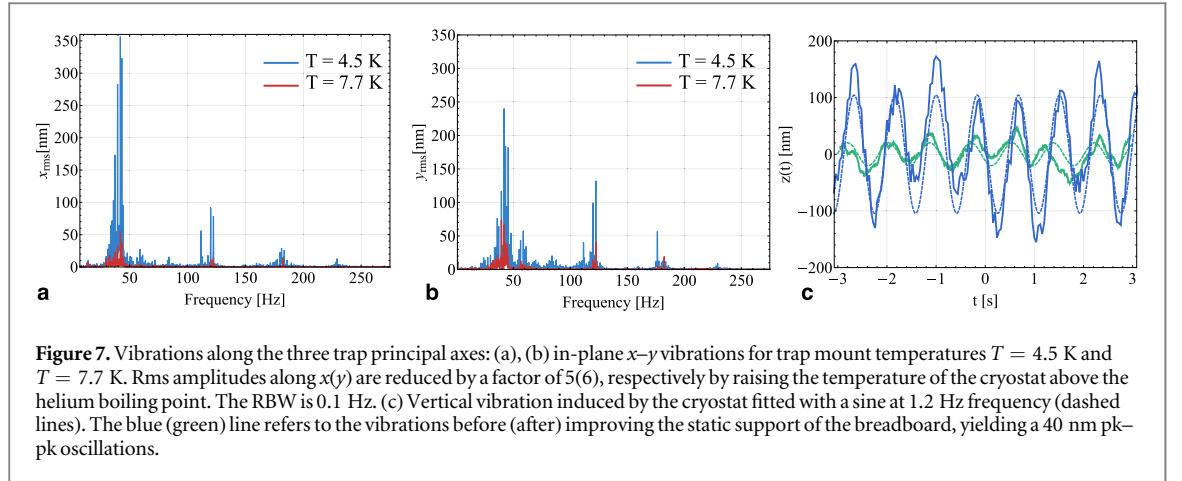
Figure 6. Interferometric setup for vibration measurements: three mirrors are mounted inside the cryostat and attached to the trap mount along the three principal axes of the trap. Three different fibers deliver laser light to three interferometers with piezo-mounted mirrors (PZT) which lock the photodiode signal to a fringe with a feedback loop. The PID voltages output to the piezos compensate for vibrations and are used to monitor their amplitude and frequency.

In the x–y plane, we observe that the main contribution is given by a peak around 40 Hz, which is attributed to the normal mode of the cryostat 60 cm long lever arm. Finite element analysis suggests that the vibration modes at higher frequencies (120 and 282 Hz peaks) are to be attributed to the mechanical structure inside the 4 K shield, made up of the resonator and the trap mount. We noticed that most of these vibrations were driven by the vibrating cold head through liquid helium condensed at the bottom of the exchange gas region at the lowest operating temperature (see figure 1(b)). This condensation results in a reduced performance of the VIS, which can be overcome by heating up the 4 K stage and operating above the He boiling point. With the 4 K stage at $T = 7.7$ K, the rms displacements in both the x and y directions are reduced by a factor of 5, as shown in figure 7. The vibration modes above 100 Hz are the most problematic ones as they are on a similar timescale of a typical quantum simulation experiment. In order to eliminate these higher frequency modes, we strengthened the resonator static support, making the whole 4 K structure stiffer. By doing so, we were able to suppress the higher frequency modes by more than an order of magnitude (see figure 8). This leaves only two very well defined normal modes at 39 and 45 Hz, which have been also suppressed with respect to figure 7(b). These lower frequency vibration modes constitute a manageable problem for our typical experiment duration as we could apply spin-echo schemes to compensate the unwanted 40 Hz phase variation. In addition, we designed a permanent mirror holder compatible with the trap in order to monitor in real time the vibrations along the Raman y direction. In this way it will be possible to compensate the unwanted phase shift via a feed-forward to the AOM phase or to an EOM in the Raman path. Alternatively, we could drive the spin–spin interactions using a phase insensitive scheme [30] to compensate passively the phase noise induced by residual mechanical vibrations (see section 4).

We also investigated the mechanical stability along the vertical z direction, finding a very well defined oscillation at the cold head vibration frequency (1.2 Hz) with a peak-to-peak amplitude of 200 nm, as shown in figure 7(c). We ascribed this almost entirely to a vibrational mode of the whole breadboard on which the cryostat is sitting. Indeed, we observe exactly the same oscillation using a reference mirror attached underneath the breadboard, instead of the mirror attached to the trap mount inside the cryostat. In order to reduce these slow oscillations, we added more static support to the elevated breadboard and thus reduced the peak-to-peak amplitude to about 40 nm. We will see in the next section how mechanical vibrations do not limit the capability of the apparatus to perform both one qubit rotations and entangling operations.

4. Coherent qubit manipulations

We designed a Raman setup to coherently manipulate ^{171}Yb$^+$ clock qubits and to perform entangling operations. The qubit is encoded in the two hyperfine clock states $|^2S_{1/2}F = 0, m_F = 0\rangle$ and $|F = 0, m_F = 1\rangle$,

Figure 7. Vibrations along the three trap principal axes: (a), (b) in-plane x–y vibrations for trap mount temperatures $T = 4.5$ K and $T = 7.7$ K. Rms amplitudes along $x(y)$ are reduced by a factor of 5(6), respectively by raising the temperature of the cryostat above the helium boiling point. The RBW is 0.1 Hz. (c) Vertical vibration induced by the cryostat fitted with a sine at 1.2 Hz frequency (dashed lines). The blue (green) line refers to the vibrations before (after) improving the static support of the breadboard, yielding a 40 nm pk–pk oscillations.

Figure 8. Improved vibrations along the y axis: after improving the resonator static support structure, the frequency modes above 100 Hz shown in figure 7(b) are suppressed by a factor of 10. The dominant acoustic modes remaining after the improvement are at 39 and 45 Hz. For both datasets, $T = 4.5$ K. The RBW is 0.1 Hz.
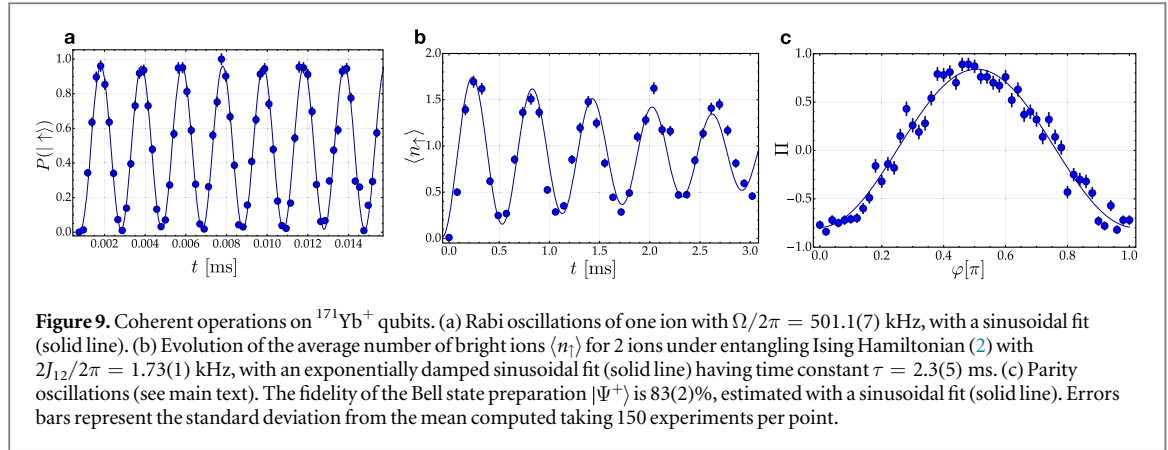
which are addressed with two counterpropagating off-resonant global laser beams at 355 nm driving stimulated Raman transitions resulting in coherent qubit rotations (see figure 9(a)). The two beams wavevector difference Δk is aligned along the y direction (see figure 4), addressing only transverse normal modes of motion through a spin dependent dipole force. We apply a bichromatic drive with two beatnotes tuned near the transverse upper and lower motional sideband frequencies at $\omega_y \pm \mu$. This gives rise in the Lamb–Dicke regime to the Ising-type Hamiltonian [3]:

$$H = \sum_{i<j} J_{ij} \sigma_i^x \sigma_j^x, \quad J_{ij} = \Omega^2 \omega_R \sum_m \frac{b_{im} b_{jm}}{\mu^2 - \omega_m^2}, \tag{2}$$

where Ω is the global (carrier) Rabi frequency, $\omega_R = \hbar \Delta k^2 / (2 M_i)$ is the recoil frequency, b_{im} is the normal mode transformation matrix of the ith ion with the mth normal mode ($\sum_i |b_{im}|^2 = \sum_m |b_{im}|^2 = 1$), M_i is the mass of a single ion and ω_m is the frequency of the mth normal mode. The minimal experiment to measure the Ising coupling is to trap two ions and let them evolve under the bichromatic Raman drive with $\mu - \omega_y \gg \eta\Omega$, where $\eta = \sqrt{\omega_R / \omega_y}$ is the Lamb–Dicke parameter. Initializing the two ions in $|\!\downarrow\downarrow\rangle_z$ and applying Hamiltonian (2) $H = J_{12} \sigma_1^x \sigma_2^x$, it is possible to observe oscillations between the two qubit states $|\!\downarrow\downarrow\rangle_z \leftrightarrow |\!\uparrow\uparrow\rangle_z$ (see figure 9(b)). In order to verify entanglement and measure off-diagonal elements of the density matrix, we stop the evolution at $t = \pi/4 J_{12}$ in order to prepare the Bell state $|\Psi^+\rangle = 1/\sqrt{2} \left(|\!\downarrow\downarrow\rangle_z + i |\!\uparrow\uparrow\rangle_z \right)$ and apply $\pi/2$ qubit analysis pulse with a varying phase φ with respect to the bichromatic drive (see figure 9(c)). This allows the measurement of the parity $\Pi = P_{\uparrow\uparrow} + P_{\downarrow\downarrow} - P_{\uparrow\downarrow} - P_{\downarrow\uparrow}$ [31], where $P_{\sigma\sigma'}$ is the probability of observing $|\sigma\sigma'\rangle$ state, with $\sigma, \sigma' = \uparrow, \downarrow$. From the parity fringe contrast (see figure 9(c)), we can extract an entanglement fidelity of 83%. This measurement certifies that the mechanical vibrations are not limiting the performance of the cryogenic quantum simulator, since are on a slower scale than typical $1/J_{ij}$ timescales. The coherence time is comparable to the one

Figure 9. Coherent operations on ^{171}Yb$^+$ qubits. (a) Rabi oscillations of one ion with $\Omega/2\pi = 501.1(7)$ kHz, with a sinusoidal fit (solid line). (b) Evolution of the average number of bright ions $\langle n_\uparrow \rangle$ for 2 ions under entangling Ising Hamiltonian (2) with $2J_{12}/2\pi = 1.73(1)$ kHz, with an exponentially damped sinusoidal fit (solid line) having time constant $\tau = 2.3(5)$ ms. (c) Parity oscillations (see main text). The fidelity of the Bell state preparation $|\Psi^+\rangle$ is 83(2)%, estimated with a sinusoidal fit (solid line). Errors bars represent the standard deviation from the mean computed taking 150 experiments per point.

of the UHV apparatus [11] and it is limited by beam pointing noise, laser intensity noise and trap frequency fluctuations. The first two sources of noise cause fluctuations in the Rabi frequency Ω, which affect both one qubit rotations and the spin–spin interactions. On the other hand trap frequency fluctuations affect the stability of the spin–spin couplings in the presence of residual entanglement between motional and spin degrees of freedom, resulting in effective spin decoherence.

It shall be noticed that coupling to the transverse normal modes [32] to generate the spin–spin coupling is more suitable for large chains (see figure 4) compared to the axial modes. Indeed with >50 ions the axial frequency has to be lowered to around 100 kHz in order to keep the ion crystal linear (see section 5 for details), given a radial trap frequency of about 4 MHz. At these low frequencies the heating rate might become problematic even at cryogenic temperatures. We estimate an axial heating rate of about 800 quanta s^{-1} for $\omega_x/2\pi \simeq 140$ kHz axial frequency, based on the measured radial heating rates [33] of 5 quanta s^{-1} at $\omega_{tr}/2\pi = 4.166$ MHz.

5. Characterization of cryogenic vacuum

The background pressure requirements for ion trap experiments are demanding primarily for two reasons. First, the ions interact with the residual neutral molecule gas with the long range $\sim r^{-4}$ potential, which increases the collision rate compared to e.g. neutral–neutral collisions rates, governed by Van-der-Waals $\sim r^{-6}$ potentials. Secondly, since the Paul trap is not static, the collisions with a bath of neutral particles can induce heating by displacing the ions diabatically with respect to typical rf timescales, depending on the mass imbalance and on the instantaneous rf phase at which the collision occurs [34–36]. As a consequence of this instantaneous and random amplification of the ion motion, the ion crystal melts, avalanche rf heating takes place, and the ions are either ejected out of the trap or left in highly excited orbits where laser cooling is inefficient. The ion chain lifetime depends strongly on the Mathieu parameter $q \simeq 2\sqrt{2}\,\omega_{tr}/\Omega_{rf}$ of the trap in consideration: once one ion is displaced by a collision, nonlinearity coming from the Coulomb repulsion will cause the ion's kinetic energy to grow at a rate that scales as a power law of q with an exponent greater than or equal to 4 [37]. The q parameter sensitivity is also related to higher order terms in the rf trapping potential expansion beyond the first order quadrupolar contribution. These terms are associated with nonlinear resonances inside the stability region of a linear Paul trap [38, 39] that are likely to accelerate the ion loss once the crystal has melted. We can qualitatively estimate, from kinematic considerations, the energy acquired by an ion i at rest after an elastic collision with a background molecule with incoming energy E_m:

$$\Delta E_i = \frac{4\xi}{(1+\xi)^2}\sin^2(\theta_{sc}/2)E_m, \tag{3}$$

where $\xi = M_m/M_i$ is the mass-imbalance parameter and θ_{sc} is the scattering angle (for details, see aappendix B). In both a room-temperature UHV system and a cryogenic apparatus, the residual background gas is made mostly of hydrogen molecules (H$_2$), the least efficiently cryo-pumped gas after helium, leading to $\xi = 0.011$ for ^{171}Yb$^+$ ions. Considering the thermal energy of H$_2$ molecules $\langle E_{H_2} \rangle = 3/2\,k_B \times 4.5$ K, we obtain, averaging over impact parameters, a mean ion energy increase of $\langle \Delta E_{Yb^+} \rangle \simeq k_B \times 150$ mK per elastic collision.

In this cryogenic vacuum system, we have not observed a catastrophic ion loss induced by collisions, even for chains of above 100 ions at $q = 0.35$. In the room temperature UHV experiment, with same q, the lifetime of a chain of about 50 ions is on average 5 min [11]. We can attribute the enhanced lifetime to two factors: on one hand differential cryo-pumping allows us to reduce the residual gas density with respect to standard UHV systems, therefore reducing the overall collision rate. Secondly, even when a collision occurs, the average energy

transfer $\langle\Delta E_{Yb^+}\rangle$ is about 60 times lower than in a room temperature UHV experiment, and therefore the crystal melting is less likely to happen as the Doppler cooling laser can efficiently recapture and recrystalize the ions. We notice that in a UHV apparatus $\langle\Delta E_{Yb^+}\rangle \simeq k_B \times 10$ K for H_2 molecules, which, according to our numerical simulations, is not sufficient to displace the ions enough to melt the crystal. According to numerical simulations (see appendix C), catastrophic collisions in a room temperature UHV system are most likely caused by rare collisions with heavier residual background gases (N_2, CO_2 and H_2O), that in a cryogenic system are completely frozen.

In order to quantify the background pressure in the vacuum system, we could not use a hot cathode ionization gauge as it can generate additional gas load. Moreover, the gauge in use measures the pressure of the room temperature vacuum region (see figure 1(b)), which is on the order of low 10^{-9} Torr when the apparatus is cold. Since both the 40 and the 4 K cryogenic regions are not vacuum sealed, it is difficult to estimate the differential cryo-pumping between the room temperature region and the inner part of the apparatus. For this reason, we used the ion crystal as a pressure gauge by measuring collision rates with the molecular hydrogen background gas as a function of the cryostat temperature.

The ion-neutral molecule interaction is described by a $\sim r^{-4}$ potential, stemming from the interaction between the charge e of the ion and the induced electric dipole moment of the molecule with static polarizability α:

$$U(r) = -\frac{\alpha}{2}\frac{e^2}{4\pi\varepsilon_0 r^4} = -\frac{C_4}{r^4}. \tag{4}$$

We can safely assume the validity of the classical Langevin model [40] with no quantum corrections, since the average energy of the incoming H_2 molecule $\langle E_{H_2}\rangle$ is much larger than the p-wave centrifugal barrier associated with the potential (4), which can be approximated as $E_4 = \hbar^2/2\mu R_4^2 \simeq k_B \times 3$ mK, with $R_4 = (2\mu C_4/\hbar^2)^{1/2}$ and μ the reduced mass [41].

In the Langevin model the collision rate γ is independent of the energy of the incoming particle and it is directly proportional to the density n, or equivalently to the pressure P assuming the ideal gas law. This results in:
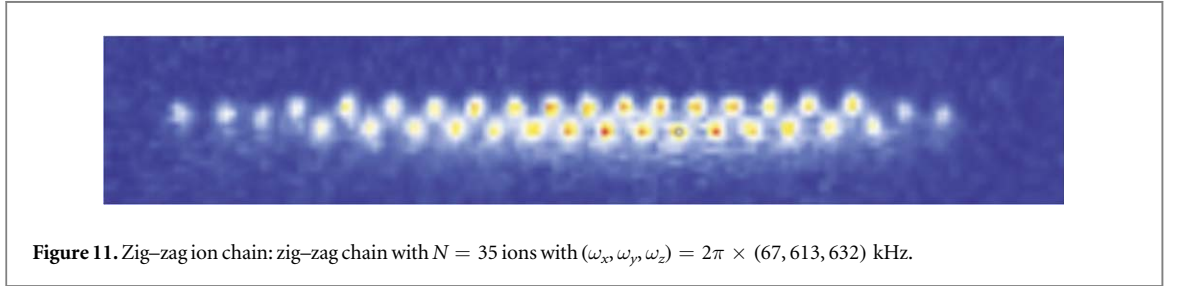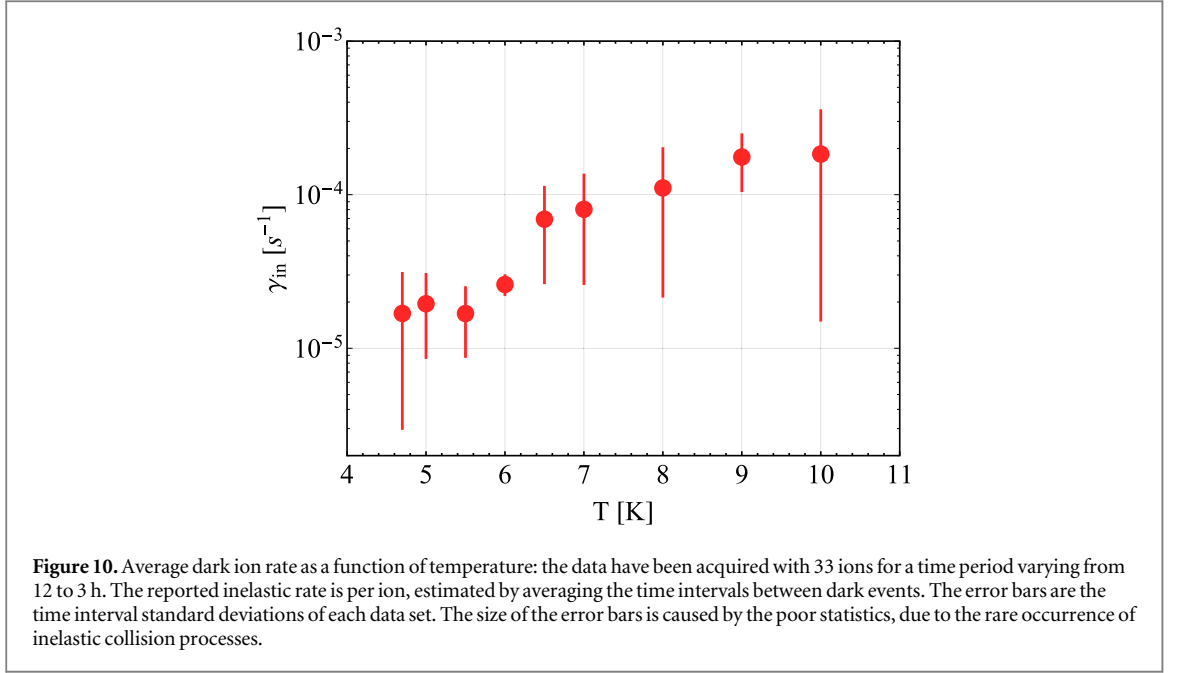
$$\gamma = n\, e\sqrt{\frac{\alpha_{H_2}\pi}{\mu\,\varepsilon_0}}, \quad n = \frac{P}{k_B T}. \tag{5}$$

In order to estimate the residual background pressure inside the cryostat, we measured the rate at which dark ions are produced. Indeed, whenever a collision occurs, there is a finite unknown probability P_{in} that two inelastic processes take place: (a) optically excited ions $^{171}Yb^{*+}$ in the $^2P_{1/2}$ or $^2D_{3/2}$ states, both populated by the Doppler cooling light at 369 nm, are subjected to collisional quenching that leads to population trapping in the metastable $^2F_{7/2}$ state [42]. (b) Molecule association: an optically excited ion has enough energy to chemically react with H_2, breaking its bond and forming an ytterbium hydride (YbH^+) molecule [43]. In both cases the ions stop scattering Doppler cooling photons and appear as missing in the ion chain as imaged on an EMCCD camera (Andor iXon 897). Therefore, we can extract a relative measurement of the pressure by recording the occurrence rate of dark ions, namely $\gamma_{in} = P_{in}\gamma$. We measured the dark ion rate as a function of the temperature of the cryostat (see figure 10) observing an increase by an order of magnitude, with a temperature increase of 5.5 K. By comparing the dark ion rate in the cryogenic vacuum system with the room temperature UHV system with a gauge-measured pressure of 1×10^{-11} Torr and $\gamma_{in}^{(300K)} = 2 \times 10^{-4}$ s^{-1} per ion, we can infer the residual background pressure as:

$$P_{4K} = P_{300K}\frac{\gamma_{in}^{(4K)}}{\gamma_{in}^{(300K)}}\frac{k_B T_{4K}}{k_B T_{300K}}. \tag{6}$$

With this method, we estimate $P_{4K} < 10^{-13}$ Torr.

In order to measure the pressure, we also considered the rate of reconfiguration events γ_{el} caused by elastic collisions when N ions are in a zig–zag configuration [44], namely when $\omega_{y,z}/\omega_x < N/\sqrt{\log(N)}$, where $\omega_{y,z}$ are the two transverse frequencies and ω_x is the axial frequency (see figure 11). When this condition is met, there are two degenerate configurations separated by a small energy gap, which depends on the transverse mode splitting $\Delta\omega_{tr} = \omega_z - \omega_y$. When an elastic collision occurs, the ions have a finite probability to switch from the 'zig' to the 'zag' configuration, if the energy gained by the ions is enough to overcome the barrier. Therefore, our observable is $\gamma_{el} = p_{flip}\gamma$, where p_{flip} is the probability of flipping the zig–zag chain, which is a function of the transverse mode splitting $\Delta\omega_{tr}$ and of the energy of the incoming particles. In order to calculate p_{flip}, we performed a numerical simulation of 31 ions in a Paul trap after a collision with a H_2 molecule with mean energy $\langle E_{H_2}\rangle = 3/2k_B T$ over 2×10^4 rf periods, calculating the probability dependence on the temperature and on the energy barrier (for details, see appendix C). The elastic rate γ_{el} has been measured at $\Delta\omega_{tr} = 2\pi \times 2$ kHz at two different temperatures ($T = 4.7$ K and the $T = 7$ K). By inverting equation (5) and using the calculated p_{flip} values, the pressure has been measured to be $P = (1 \pm 1) \times 10^{-12}$ Torr and $P = (2 \pm 1) \times 10^{-12}$ Torr for $T = 4.7$ K and 7 K, respectively.

Figure 10. Average dark ion rate as a function of temperature: the data have been acquired with 33 ions for a time period varying from 12 to 3 h. The reported inelastic rate is per ion, estimated by averaging the time intervals between dark events. The error bars are the time interval standard deviations of each data set. The size of the error bars is caused by the poor statistics, due to the rare occurrence of inelastic collision processes.

Figure 11. Zig–zag ion chain: zig–zag chain with $N = 35$ ions with $(\omega_x, \omega_y, \omega_z) = 2\pi \times (67, 613, 632)$ kHz.

6. Uniformly spaced ion-chains

The segmented blade trap features 10 static electrodes which allow for the realization of axial anharmonic potentials. In particular, quartic axial potentials have been shown to offer several advantages in handling, cooling [45] and performing coherent operations [46] on large ion chains. Such potentials relax the conditions necessary to achieve a linear configuration of the ion chain, avoiding zig–zag transitions at the center of the chain. At the same time, tailored anharmonicity in the axial potential allows us to minimize the ion spacing inhomogeneity induced by the Coulomb repulsion and enables control of the average spacing between the ions. In addition, a homogeneous spacing configuration prevents the ions in the chain center from coming too close to each other, which reduces cross-talk in ion state detection and single ion manipulation with focused laser beams. Finally, the anharmonic potentials can be used to shape the normal mode structure [47, 48] and to minimize the inhomogeneity in the laser-induced spin–spin coupling [2] by shaping the transverse normal-mode dispersion.
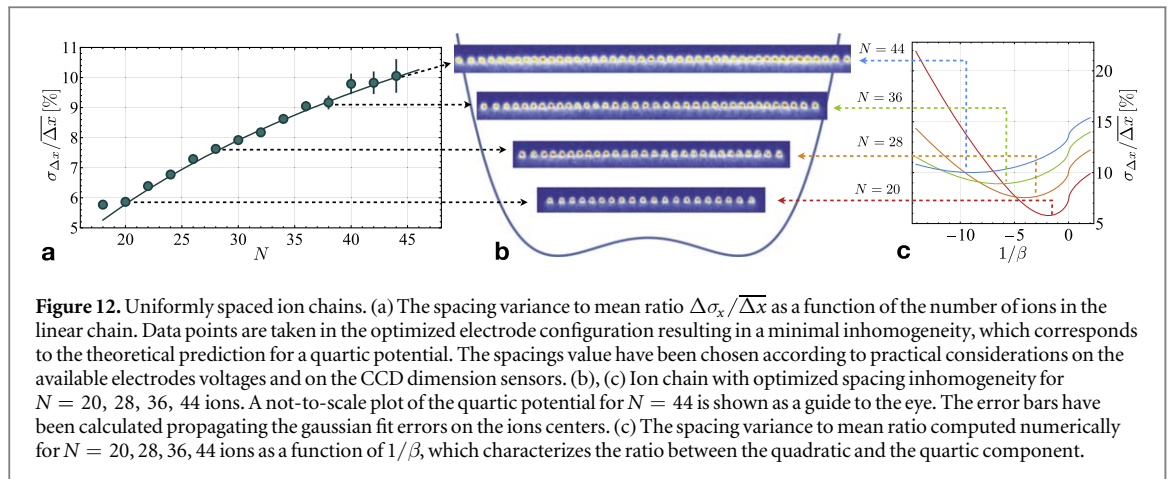
The form of the quartic axial potential induced by the static electrodes can be written as:

$$V_{ax} = \sum_{i=1}^{N} \frac{\alpha_2}{2} x_i^2 + \frac{\alpha_4}{4} x_i^4, \tag{7}$$

where x_i is the position of the ith ion and $\alpha_2 = m\omega_x^2$, with ω_x the axial frequency and m the ion atomic mass. The axial equilibrium positions are determined by the balance between the electrostatic axial forces ($F_{ax} = -\partial_x V_{ax}$) and the inter-ion Coulomb repulsion:

$$0 = u_i + \beta u_i^3 - \sum_{j=1}^{i-1} (u_i - u_j)^{-2} + \sum_{j=i+1}^{N} (u_i - u_j)^{-2}, \tag{8}$$

where $u_i = x_i/\ell$ is the ith ion's position in adimensional units and $\ell = (q^2/4\pi\epsilon_0 m\omega_x^2)^{1/3}$ is the characteristic length of the axial potential, with ϵ_0 the vacuum permittivity and q the electron charge. The quartic potential is characterized by the dimensionless ratio $\beta = \alpha_4 \ell^2 / \alpha_2$ [46], which can be optimized to minimize the

Figure 12. Uniformly spaced ion chains. (a) The spacing variance to mean ratio $\Delta\sigma_x/\overline{\Delta x}$ as a function of the number of ions in the linear chain. Data points are taken in the optimized electrode configuration resulting in a minimal inhomogeneity, which corresponds to the theoretical prediction for a quartic potential. The spacings value have been chosen according to practical considerations on the available electrodes voltages and on the CCD dimension sensors. (b), (c) Ion chain with optimized spacing inhomogeneity for $N = 20, 28, 36, 44$ ions. A not-to-scale plot of the quartic potential for $N = 44$ is shown as a guide to the eye. The error bars have been calculated propagating the gaussian fit errors on the ions centers. (c) The spacing variance to mean ratio computed numerically for $N = 20, 28, 36, 44$ ions as a function of $1/\beta$, which characterizes the ratio between the quadratic and the quartic component.

inhomogeneity of the ion chain. By solving equation (8), it is possible to find the optimal $\beta^*(N)$ (see figure 12(c)) for a certain ion number *N*, that minimizes the ion inhomogeneity which can be parameterized by the ratio $\sigma_{\Delta x}/\overline{\Delta x}$, where $\sigma_{\Delta x}$ and $\overline{\Delta x}$ are the ion spacing standard deviation and mean spacing, respectively. Once the optimal $\beta^*(N)$ is found, it is possible to fully determine the potential by choosing a desired average spacing $\overline{\Delta x}$, which depends on the absolute value of the harmonic frequency ω_x. A particular choice of the quadratic term α_2^* determines the characteristic length $\ell(\alpha_2^*)$ and corresponds to a certain equilibrium average spacing $\overline{\Delta x}^*$. Therefore, the quartic component is univocally determined by the equation $\alpha_4 = \beta^*\alpha_2^*/\ell(\alpha_2^*)$. In figure 12(a), it is shown how we can obtain the minimum variance to mean spacing ratio (solid curves) by tuning the quartic potential, ranging from $N = 18$ to $N = 44$ ions in a linear configuration.

7. Conclusions

In this work we have reported on a new cryogenic ion trap experimental apparatus designed for large scale quantum simulation of spin models. We designed and optimized the system to routinely trap over 100 ions in a linear chain and hold them for hours. We improved the system's mechanical stability, characterized the residual background pressure by measuring the inelastic and elastic collision rate with H_2 molecules and used anharmonic potentials to achieve uniformly spaced ion chains. In the short term we plan to address the ions with global Raman beams, inducing tunable spin–spin interaction with power law range [2] and to study the dynamics of the system after a quantum quench. In order to compute the exact dynamics in this diabatic regime it is necessary to consider a large fraction of the Hilbert space, which grows exponentially with the system size. Given the measured coherence time, we anticipate the ability to perform quantum simulations with over 100 ions, following a recent simulation with up to 53 ions in a room temperature UHV apparatus [6].

This apparatus is also well-suited for implementing single ion addressability using individual light shifts from a laser focused on the ions [49] through the high numerical aperture window already used for imaging. This tool can be used to realize disordered potentials on the ions or to prepare arbitrary initial product states. In the long run it is possible to envision single ion addressability also for the entangling operations shown in section 4, by inserting a small objective in the 4 K region, close to the trap. This would pave the way also for digital protocols for both quantum simulation and computation, making this apparatus an ideal test-bed to investigate both quantum algorithms and simulation of synthetic quantum matter with a number of qubits impossible to simulate exactly on a classical computer.

Acknowledgments

Appendix A. Heat load budget

Component	$\dot{Q}_{40K}$ (W)	$\dot{Q}_{4K}$ (mW)
40 K shield	5.6	—
4 K shield	—	1
2″ viewport	0.8	0.6
1″ viewports	1.6	1.2
Wiring	0.5	220

Appendix B. Ion–molecule collision

Let us consider the $1/r^4$ polarization interaction between the ion and the neutral molecule. Suppose the reduced mass is $\mu = m_1 m_2/(m_1 + m_2)$, angular momentum L and energy E in the center of mass frame, and the attractive potential $U(r) = -C_4/r^4$, where $C_4 = \alpha e^2/8\pi\varepsilon_0$. They are related to the initial velocity v_0 and the impact parameter b in the lab frame as $L = b\mu v_0$ and $E = \frac{1}{2}\mu v_0^2$. We can use the Binet equation to solve the shape of the orbit [40]:

$$\theta = \int \frac{L\,\mathrm{d}u}{\sqrt{2\mu(E + C_4 u^4) - L^2 u^2}}, \tag{B.1}$$

where $u \equiv 1/r$. Here we are interested in the scattering angle of the particles:

$$\pi - \theta_s = 2\int_0^{u_0} \frac{L\,\mathrm{d}u}{\sqrt{2\mu(E + C_4 u^4) - L^2 u^2}}, \tag{B.2}$$

where

$$u_0 = \sqrt{\frac{L^2 - \sqrt{L^4 - 16 C_4 \mu^2 E}}{\alpha\mu}} \tag{B.3}$$

corresponds to the inverse minimal distance between the two particles. After some algebra we get

$$\theta_{\mathrm{sc}} = \pi - \frac{2\sqrt{2}\,K\left(\frac{1-x}{1+x}\right)}{\sqrt{1+x}}, \tag{B.4}$$

where $x = \sqrt{1 - \frac{16 C_4 \mu^2 E}{L^4}}$ and $K(m)$ is the complete elliptic integral of the first kind. In the limit $C_4 \to 0$ we have $\theta_s \to 0$. Note that this expression works only if $16 C_4 \mu^2 E < L^4$, otherwise the two particles will really collide as they approach each other. This condition defines a critical impact parameter $b_c = (8C_4/\mu v_0^2)^{1/4}$. Finally, the velocity of the ion in the lab frame, which is originally 0, becomes
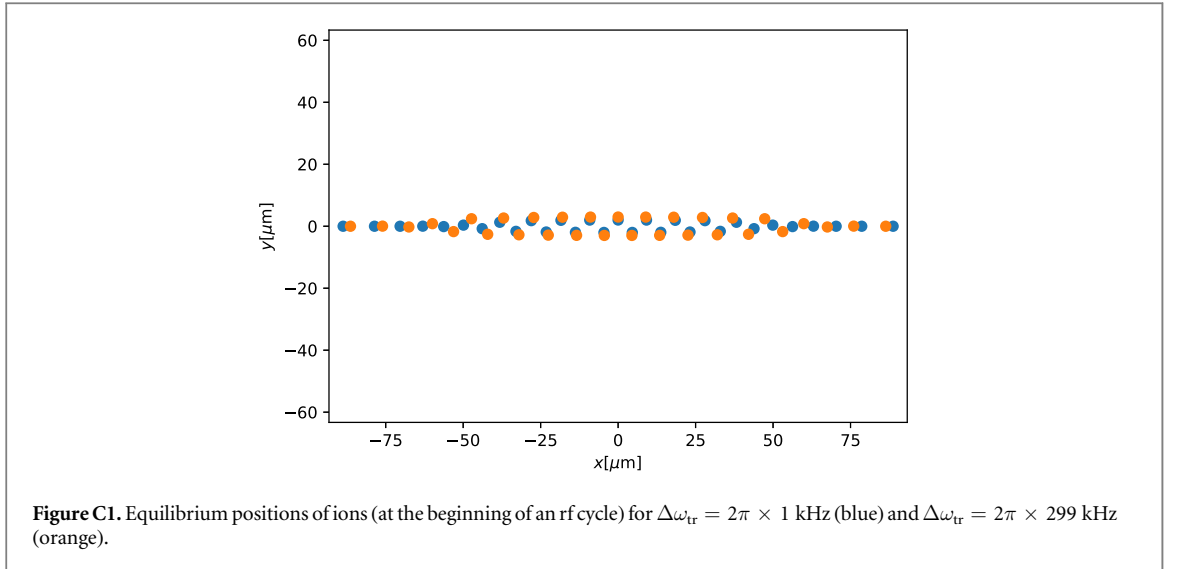
$$v_x = \frac{M_m}{M_i + M_m} v_0 (1 - \cos\theta_{\mathrm{sc}}), \tag{B.5}$$

$$v_y = -\frac{M_m}{M_i + M_m} v_0 \sin\theta_{\mathrm{sc}}. \tag{B.6}$$

In the $16 C_4 \mu^2 E > L^4$ case, as mentioned above, the two particles will keep being attracted to each other. The rotation angle when they overlap is

$$\theta = \int_0^\infty \frac{\mathrm{d}x}{\sqrt{1 - x^2 + \frac{4 C_4 \mu^2 E}{L^4} x^4}}, \tag{B.7}$$

leading to $\theta_{\mathrm{sc}} = \pi - 2\theta$. For the following numerical simulation, we considered $\theta_{\mathrm{sc}} = \pi$ for simplicity. This will overestimate by a factor of order one the energy transferred to the ion for $b < b_c$. However, as we truncate the impact parameter at b_c, we are also underestimating the energy transfer for $b > b_c$. Therefore the overall effect of this simplification should not be significant. For a more rigorous treatment, it would be required to integrate over the impact parameter to get the average amount of energy transfer in the collision, or sample directly the impact parameter for each simulation to find the energy of the ion after the collision.

Figure C1. Equilibrium positions of ions (at the beginning of an rf cycle) for $\Delta\omega_{\text{tr}} = 2\pi \times 1$ kHz (blue) and $\Delta\omega_{\text{tr}} = 2\pi \times 299$ kHz (orange).

Appendix C. Numerical simulation of a zig–zag ion chain

Let us consider a trap with $\Omega_{\text{rf}} = 2\pi \times 24$ MHz and $\omega_x = 2\pi \times 67$ kHz, $(\omega_y + \omega_z)/2 = 2\pi \times 622.5$ kHz. For $N = 31$ ions and transverse splitting up to $\Delta\omega_{\text{tr}}/2\pi = (\omega_z - \omega_y)/2\pi = 299$ kHz, the equilibrium positions of the ions have a zig–zag shape in the x–y plane. For example, figure C1 shows the equilibrium positions for $\Delta\omega_{\text{tr}} = 2\pi \times 1$ kHz (blue) and $\Delta\omega_{\text{tr}} = 2\pi \times 299$ kHz (orange).
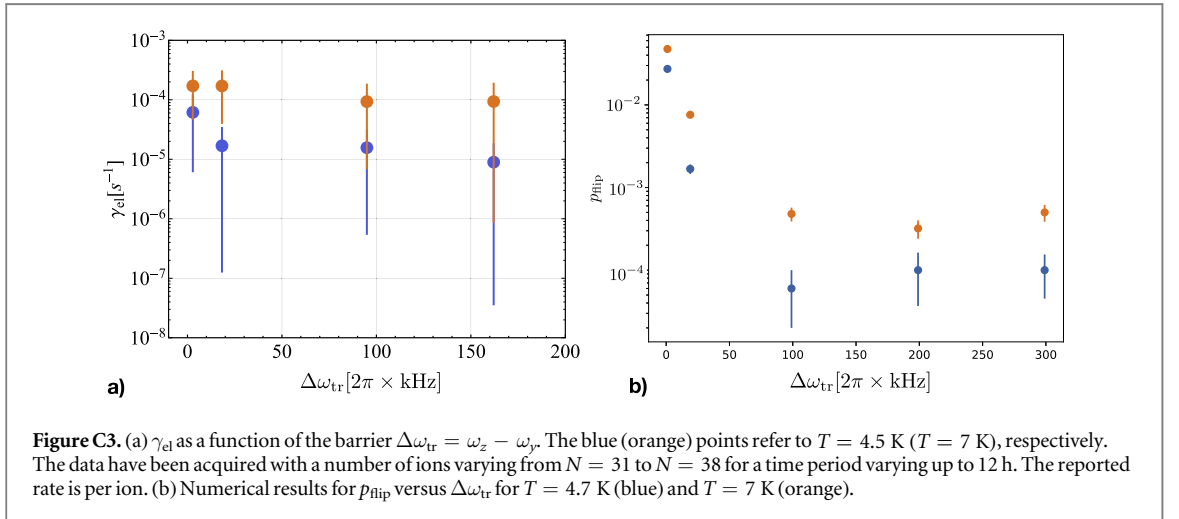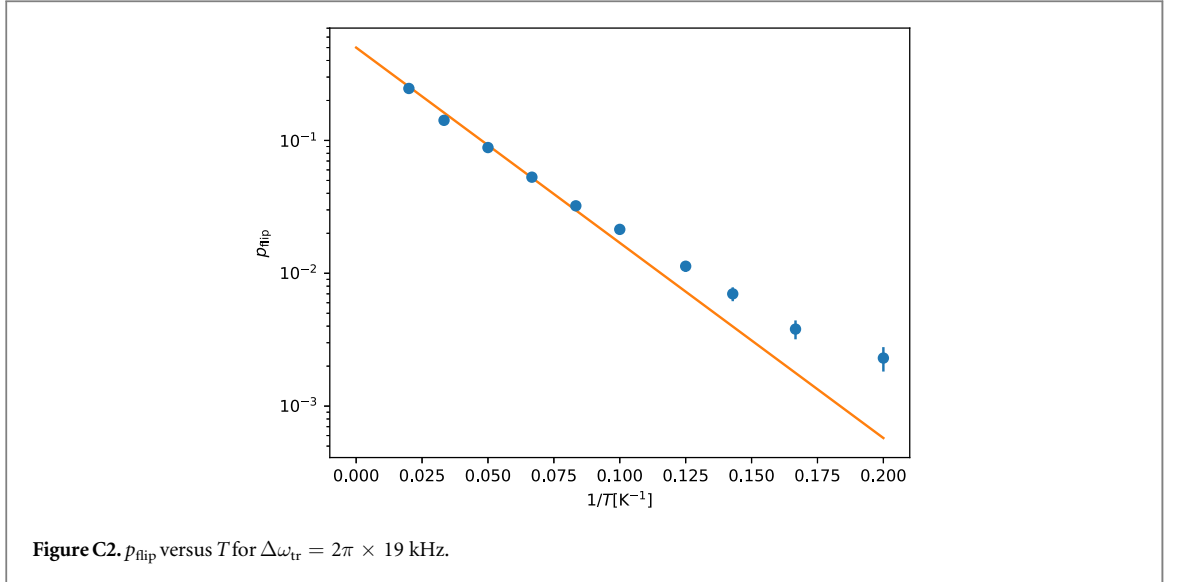
For a given $\Delta\omega_{\text{tr}}$, hence given trap parameters and equilibrium positions, we can simulate the probability for the zig–zag shape to flip after a collision with a H_2 molecule at temperature T. The velocity of H_2 follows a Maxwell–Boltzmann distribution and, as mentioned above, the collision is in 1D along the incoming direction of the molecule. Numerically, we find that after 2×10^4 rf periods the ions will reach a local potential minimum (not necessarily the original one) due to the Doppler cooling effect (see also appendix D). Then, we can compare the initial and the final configurations and see if the chain has flipped from a 'zig' to a 'zag' configuration. At low temperature such probability is very small and hence lots of samples are needed to measure it precisely. In order to count the number of flipping events, we sort the initial and the final positions respectively according to their x coordinates, and then add up the squared distances between corresponding ions. If the configuration has not flipped, the sum will be small (in our case $\lesssim 22$ μm^2); otherwise the sum will be much larger.

From the computational point of view, it has to be pointed out that the trapped ion system is chaotic because of the nonlinear Coulomb interaction, thus any computational error will accumulate exponentially with the evolution time. To suppress the error, we may need very small step length and very high numerical precision, and the simulation soon becomes computationally intractable. However, we know that in the experiment there is always a Doppler cooling beam (see appendix D for how this effect is included in the simulation) and that the scattering of the photons itself is random. Therefore small errors in the simulation shall not change the qualitative behavior. For the simulations we use Forest-Ruth method with 100 steps per rf period and *double* precision. We checked p_{flip} convergence increasing from 100 to 1000 steps per RF period.

First, we study the T dependence in the probability p_{flip} by fixing $\Delta\omega_{\text{tr}} = 2\pi \times 19$ kHz. The numerical results are shown in figure C2. As we can see, for high temperature ($T \gtrsim 12$ K) the probability can be modeled as $p_{\text{flip}} = 0.5 \exp(-E/T)$; but at low temperature the probability is greater than this prediction. This suggests the existence of multiple paths and hence multiple energy barriers to flip the configuration.

Next, we consider the $\Delta\omega_{\text{tr}}$ dependence at $T = 4.7$ K and $T = 7$ K, which is shown in figure C3(b). Because the probability p_{flip} is so low, we randomly sample 10^5 initial conditions to estimate the probability and repeat this process for 5 times to estimate the error bar. Note that p_{flip} does not decrease monotonically as $\Delta\omega_{\text{tr}}$ increases. This is because of the multiple modes inside the y–z plane, i.e. the previously mentioned multiple energy barriers. Also note that at large $\Delta\omega_{\text{tr}}$ it is possible to flip 'half' the configuration: the ions will reach a local minimum of potential energy, but not necessarily the global minimum.

Figure C3(a) shows the elastic rate measurements as a function of the barrier $\Delta\omega_{\text{tr}}$. As the barrier increases, there is a suppression in the reconfiguration rate but not of two orders of magnitude as predicted by the theory (figure C3(b)). The discrepancy might be due to the difficulty in acquiring data for hours and in sampling such a low reconfiguration probability without having flipping events not caused by collisions. We experimentally observed that the flipping rate increases with the number of dark ions, which are only sympathetically cooled by the bright ions, leading to a higher temperature of the chain that can cause the thermal activation of the flipping

Figure C2. p_{flip} versus T for $\Delta\omega_{\text{tr}} = 2\pi \times 19$ kHz.

Figure C3. (a) γ_{el} as a function of the barrier $\Delta\omega_{\text{tr}} = \omega_z - \omega_y$. The blue (orange) points refer to $T = 4.5$ K ($T = 7$ K), respectively. The data have been acquired with a number of ions varying from $N = 31$ to $N = 38$ for a time period varying up to 12 h. The reported rate is per ion. (b) Numerical results for p_{flip} versus $\Delta\omega_{\text{tr}}$ for $T = 4.7$ K (blue) and $T = 7$ K (orange).

events. Also electric field noise (not included in the simulation) at frequencies of the order of the barrier could flip the zig zag chain. These two factors probably prevent us from resolving reconfiguration rates lower than 10^{-5} s^{-1}. For these reasons the measurement of γ_{el} at the lowest barrier value $\Delta\omega_{\text{tr}}/(2\pi) = 2$ kHz is the most reliable estimate of the pressure.

Appendix D. Doppler cooling

A weak Doppler cooling beam is always on during the storage of the ion crystal. Typically, the Doppler Cooling beam at $\lambda = 369$ nm is directed along the [1, 1, 0] direction of the trap and detuned at $\Delta = -\Gamma/2$ ($\Gamma_{^2P_{1/2}} = 2\pi \times 19$ MHz in ^{171}Yb$^+$) with a saturation parameter $s = I/I_s = 1$, where $I_s = 4\pi^2\hbar c\Gamma/6\lambda^3$ is the saturation intensity. Since with these parameters the photon scattering rate is about $2\pi \times 3$ MHz and is smaller than the rf frequency of the trap, the damping force should not be modeled as a simple $-\gamma\mathbf{v}$ term. To describe the physics here we use N two-dimensional vectors to describe the internal states of the ions and consider the excitation of ions by the laser beam quantum mechanically. Then, quantum trajectory [50] method can be used to simulate the scattering process. At each step the internal state of an ion is first evolved from $|\psi(t)\rangle$ to $|\tilde{\psi}(t + \mathrm{d}t)\rangle$ under the effective Hamiltonian

$$H_{\text{eff}} = \frac{\Delta - \mathbf{k} \cdot \mathbf{v}}{2}\sigma_z + \frac{\Omega}{2}\sigma_x - \frac{i}{4}\gamma(I - \sigma_z). \tag{D.1}$$

Then, with probability $\langle\tilde{\psi}(t + \mathrm{d}t)|\tilde{\psi}(t + \mathrm{d}t)\rangle$ the internal state is renormalized to $|\psi(t + \mathrm{d}t)\rangle = |\tilde{\psi}(t + \mathrm{d}t)\rangle/\||\tilde{\psi}(t + \mathrm{d}t)\rangle\|$; otherwise a transition occurs and the ion goes back to the ground

state $|\psi(t + dt)\rangle = |0\rangle$, together with a momentum change as the ion absorbs a photon in the [1, 1, 0] direction and then emits one into a random direction.

ORCID iDs

G Pagano ⬤ https://orcid.org/0000-0002-6760-4015
P W Hess ⬤ https://orcid.org/0000-0003-2985-4221
Y Wu ⬤ https://orcid.org/0000-0003-2184-7553

References

[1] Monroe C and Kim J 2013 *Science* **339** 1164–9
[2] Porras D and Cirac J I 2004 *Phys. Rev. Lett.* **92** 207901
[3] Kim K, Chang M S, Islam R, Korenblit S, Duan L M and Monroe C 2009 *Phys. Rev. Lett.* **103** 120502
[4] Bohnet J G, Sawyer B C, Britton J W, Wall M L, Rey A M, Foss-Feig M and Bollinger J J 2016 *Science* **352** 1297–301
[5] Jurcevic P, Shen H, Hauke P, Maier C, Brydges T, Hempel C, Lanyon B P, Heyl M, Blatt R and Roos C F 2017 *Phys. Rev. Lett.* **119** 080501
[6] Zhang J *et al* 2017 *Nature* **543** 217–20
[7] Gerritsma R, Kirchmair G, Zähringer F, Solano E, Blatt R and Roos C F 2010 *Nature* **463** 68
[8] Martinez E A *et al* 2016 *Nature* **534** 516
[9] Hempel C *et al* 2018 *Phys. Rev. X* **8** 031022
[10] Toyoda K, Hiji R, Noguchi A and Urabe S 2015 *Nature* **527** 74
[11] Zhang J, Pagano G, Hess P W, Kyprianidis A, Becker P, Kaplan H, Gorshkov A V, Gong Z X and Monroe C 2017 *Nature* **551** 601
[12] Gabrielse G, Khabbaz A, Hall D S, Heimann C, Kalinowsky H and Jhe W 1999 *Phys. Rev. Lett.* **82** 3198–201
[13] Poitzsch M E, Bergquist J C, Itano W M and Wineland D J 1996 *Rev. Sci. Instrum.* **67** 129–34
[14] Labaziewicz J, Ge Y, Antohi P, Leibrandt D, Brown K R and Chuang I L 2008 *Phys. Rev. Lett.* **100** 013001
[15] Sage J M, Kerman A J and Chiaverini J 2012 *Phys. Rev. A* **86** 013417
[16] Schwarz M *et al* 2012 *Rev. Sci. Instrum.* **83** 083115
[17] Niedermayr M, Lakhmanskiy K, Kumph M, Partel S, Edlinger J, Brownnutt M and Blatt R 2014 *New J. Phys.* **16** 113068
[18] Brandl M F *et al* 2016 *Rev. Sci. Instrum.* **87** 113103
[19] Alonso J, Leupold F M, Solèr Z U, Fadel M, Marinelli M, Keitch B C, Negnevitsky V and Home J P 2016 *Nat. Commun.* **7** 11243
[20] Turchette Q A *et al* 2000 *Phys. Rev. A* **61** 063418
[21] Brownnutt M, Kumph M, Rabl P and Blatt R 2015 *Rev. Mod. Phys.* **87** 1419–82
[22] Mamun M A A, Elmustafa A A, Stutzman M L, Adderley P A and Poelker M 2014 *J. Vac. Sci. Technol. A* **32** 021604
[23] Ekin J 2006 *Experimental Techniques for Low-Temperature Measurements* (Oxford: Oxford University Press)
[24] Siverns J D and Quraishi Q 2017 *Quantum Inf. Process.* **16** 314
[25] Olmschenk S, Younge K C, Moehring D L, Matsukevich D N, Maunz P and Monroe C 2007 *Phys. Rev. A* **76** 052314
[26] Stick D, Hensinger W K, Olmschenk S, Madsen M J, Schwab K and Monroe C 2006 *Nat. Phys.* **2** 36–9
[27] Macalpine W W and Schildknecht R O 1959 *Proc. IRE* **47** 2099–105
[28] Siverns J D, Simkins L R, Weidt S and Hensinger W K 2012 *Appl. Phys. B* **107** 921–34
[29] Johnson K G, Wong-Campos J D, Restelli A, Landsman K A, Neyenhuis B, Mizrahi J and Monroe C 2016 *Rev. Sci. Instrum.* **87** 053110
[30] Inlek I V, Vittorini G, Hucul D, Crocker C and Monroe C 2014 *Phys. Rev. A* **90** 042316
[31] Sackett C A *et al* 2000 *Nature* **404** 256
[32] Zhu S L, Monroe C and Duan L M 2006 *Phys. Rev. Lett.* **97** 050505
[33] Bruzewicz C D, Sage J M and Chiaverini J 2015 *Phys. Rev. A* **91** 041402
[34] Zipkes C, Ratschbacher L, Sias C and Köhl M 2011 *New J. Phys.* **13** 053020
[35] Cetina M, Grier A T and Vuletić V 2012 *Phys. Rev. Lett.* **109** 253201
[36] Chen K, Sullivan S T and Hudson E R 2014 *Phys. Rev. Lett.* **112** 143009
[37] Ryjkov V L, Zhao X and Schuessler H A 2005 *Phys. Rev. A* **71** 033414
[38] Alheit R, Kleineidam S, Vedel F, Vedel M and Werth G 1996 *Int. J. Mass Spectrom. Ion Process.* **154** 155–69
[39] Drakoudis A, Söllner M and Werth G 2006 *Int. J. Mass Spectrom.* **252** 61–8
[40] Langevin M 1905 *Ann. Chim. Phys.* **5** 245–88
[41] Jachymski K, Krych M, Julienne P S and Idziaszek Z 2013 *Phys. Rev. Lett.* **110** 213202
[42] Lehmitz H, Hattendorf-Ledwoch J, Blatt R and Harde H 1989 *Phys. Rev. Lett.* **62** 2108–11
[43] Sugiyama K and Yoda J 1997 *Phys. Rev. A* **55** R10–3
[44] Fishman S, De Chiara G, Calarco T and Morigi G 2008 *Phys. Rev. B* **77** 064111
[45] Lin G D and Duan L M 2015 *Quantum Inf. Process.* **15** 5299–313
[46] Lin G D, Zhu S L, Islam R, Kim K, Chang M S, Korenblit S, Monroe C and Duan L M 2009 *Europhys. Lett.* **86** 60004
[47] Home J P, Hanneke D, Jost J D, Leibfried D and Wineland D J 2011 *New J. Phys.* **13** 073026
[48] Johanning M 2016 *Appl. Phys. B* **122** 71
[49] Lee A C, Smith J, Richerme P, Neyenhuis B, Hess P W, Zhang J and Monroe C 2016 *Phys. Rev. A* **94** 042308
[50] Daley A J 2014 *Adv. Phys.* **63** 77–149